



# The Effect of Ti on the Early Stages of Oxidation of an Alumina-Forming NiCrAl Alloy

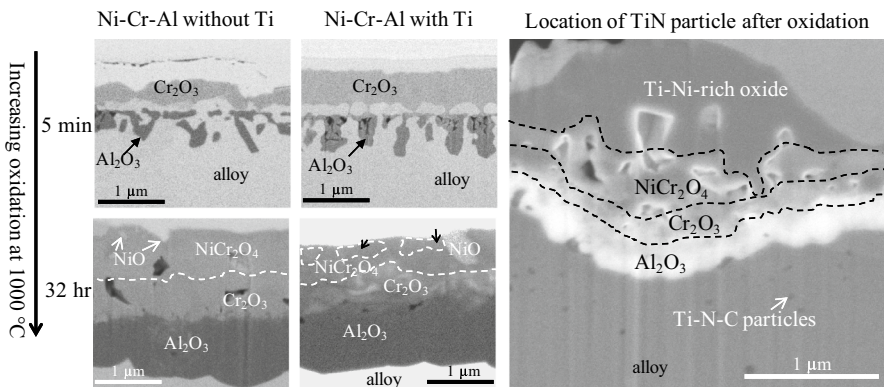
Talia L. Barth<sup>1</sup> · Emmanuelle A. Marquis<sup>1</sup>

Received: 30 September 2018 / Published online: 10 May 2019  
© Springer Science+Business Media, LLC, part of Springer Nature 2019

## Abstract

Model  $\gamma$ -NiCrAl alloys with and without titanium were oxidized for short times up to 32 h at 1000 °C and subsequently characterized by scanning electron microscopy, transmission electron microscopy, and atom probe tomography in order to clarify the role of Ti on the oxidation behavior of alumina-forming nickel alloys. At the longer oxidation times, Ti was found to have no significant effect on the major protective oxide phases formed and overall scale and individual oxide layer thicknesses. Ti was observed to segregate to interfaces within the scale and form a Ti-rich oxide at the scale surface over time. At the shortest oxidation times before a continuous  $\text{Al}_2\text{O}_3$  layer formed, the Ti-containing alloys exhibited thicker  $\text{Cr}_2\text{O}_3$  layers, suggesting that Ti accelerates  $\text{Cr}_2\text{O}_3$  growth kinetics. Additionally, oxide nodules resulting from fast oxidation of TiN particles were observed on the Ti-containing alloys. These may be linked to increased spalling propensity of Ti-containing alloys.

## Graphical Abstract



**Keywords** High-temperature oxidation · NiCrAl · Titanium · Electron microscopy · Atom probe tomography

Extended author information available on the last page of the article

## Introduction

Nickel-based alloys are used in a variety of high-temperature applications that require excellent mechanical properties. Though these materials have been developed to have superior strength, toughness, and creep resistance, they are often limited by their vulnerability to oxidation. Oxidation resistance is generally developed through the addition of aluminum and/or chromium, which tend to form dense, continuous external layers of stable  $\text{Al}_2\text{O}_3$  and  $\text{Cr}_2\text{O}_3$ . To protect the underlying alloy from further attack by oxidation, the external scale should develop quickly and then grow slowly at high temperatures. In addition, it is critical that the protective oxide scale be adherent to the underlying alloy, to avoid spallation and further attack of the alloy.

In the case of ternary Ni–Cr–Al alloys, the steady-state morphology and composition of oxide scales formed strongly depend on alloy chemistry. This correlation has been experimentally determined and mapped onto a Ni–Cr–Al ternary phase diagram [1]. For example, a continuous  $\text{Al}_2\text{O}_3$  scale requires a minimum alloy Al concentration and Cr alloying decreases this critical Al content. However, while the oxidation behavior of binary or ternary Ni–Cr–Al alloys is relatively well understood [2], the situation is quickly complicated by the addition of alloying elements. Commercial superalloys have on the order of ten or more components, and each may affect the formation and growth of oxide scales. Moreover, small amounts of dopant elements can have a significant effect on the oxidation kinetics and mechanical properties of a protective scale [3].

The contribution of alloying elements to the oxidation behavior may take several different forms. The “reactive” elements such as Y, Hf, Zr, and Ce, were found to segregate to  $\text{Al}_2\text{O}_3$  grain boundaries and reduce significant upward cation transport [3, 4]. Other elements, such as Ti in chromia, may affect bulk diffusion through the oxide scale by changing defect concentrations [5]. The so-called third element effect that describes the effect of Cr on  $\text{Al}_2\text{O}_3$  formation has been linked to a change in the activity of oxidizing elements in the alloy leading to a reduction in the critical concentration required to create a continuous oxide scale [6].

Titanium is often present as a minor alloying element in Ni-based superalloys to stabilize the  $\gamma'$  strengthening phase [7], but its effect on the oxidation response is unclear. In the case of chromia-forming alloys, faster growth kinetics were observed for chromia on a Ti-containing alloy than chromia on an un-doped alloy [8]. It was suggested that Ti acts by increasing the chromium vacancy concentration in chromia [9, 10]. The effect of titanium doping on aluminum oxide scales is less clear. On NiAl alloys that form exclusive, continuous alumina scales, titanium additions slightly reduced the alumina growth rate [11] and suppressed the surface ridge structure typical of NiAl oxidation [12]. However, Ti additions to  $\gamma$ -Ni alloys slightly increased the alumina oxidation rate while having no significant effect on other alloy compositions, suggesting that the effect of Ti doping may be dependent on the matrix composition as well as level of Ti addition [13]. In alloys containing reactive elements such as yttrium, there seems to be some synergistic

effect between the different alloying elements. In NiCrAlY alloys, titanium additions reduced the long-term oxidation rate by changing the alumina morphology and promoting a uniform and continuous scale rather than internal alumina oxidation [14]. In FeCrAlY alloys, Ti + Y co-doping led to a slight decrease in oxidation rate as compared to the solely Y-doped alloy [15]. The microstructures of the Y-doped and Y + Ti-doped alloys were similar, but in the Ti-doped scale, no Y-rich oxide precipitates were observed, while yttrium oxides were found in the scale grown on the Ti-free alloy, implying that titanium might affect the distribution of yttrium throughout the oxide scale. Additionally, Ti was found to segregate to grain boundaries in alumina scales, with more Ti present at the top of the scale than at the scale–alloy interface, suggesting that Ti diffuses upward through the scale along the interfaces [16], similar to the “reactive element” type effect. However, from the current literature, it is still unclear how Ti alone affects the kinetics and early development of protective oxide scales.

The variety of alloy compositions used in prior studies has limited our understanding of the exact role of Ti on the oxidation of alumina-forming Ni alloys. Therefore, the goal of this study is to isolate the effect of titanium on the oxidation behavior of a model Ni–Cr–Al alloy by performing detailed microstructural characterization of the oxide scales as they develop at short oxidation times.

## Experimental Procedures

Four alloys were considered in this study. Alloy 1 was Ti-free and selected so that the  $\gamma$ -Ni phase was the only stable phase at the oxidation temperature of 1000 °C (Fig. 1) while forming a continuous  $\text{Al}_2\text{O}_3$  scale (region III) [1]. Two Ti-containing alloys (Alloys 2 and 3) with the same Cr and Al concentrations (26 and 10 at.%, respectively) as the reference Alloy 1 were also used. Alloy 2 contained 0.6 at.% Ti and Alloy 3 1.7 at.% Ti. Alloys 1, 2, and 3 were cast using a Bridgeman furnace,

**Fig. 1** Ni–Cr–Al phase diagram (at.%) at 1000 °C calculated in ThermoCalc using the TCNI8 superalloys database, v8.1. The red star shows the location of the nominal base alloy (Ni–26Cr–10Al), and the blue star shows the nominal high-Al alloy (Ni–26Cr–12Al). The green and blue highlighted areas and lines represent the  $\gamma + \gamma'$  phase fields for the +0.6Ti and +1.7Ti alloys, respectively (Color figure online)

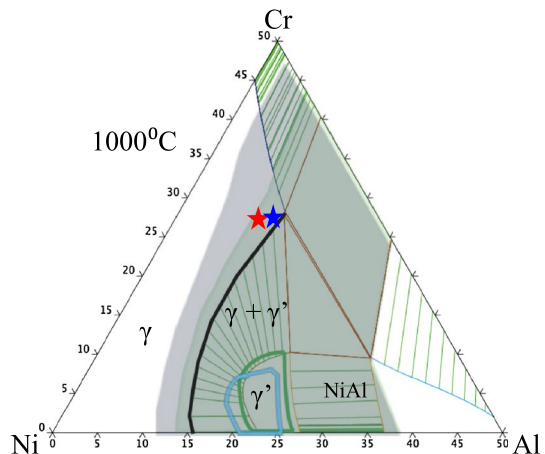


**Table 1** Nominal alloy compositions in at.%

ID	Ni	Cr	Al	Ti
Alloy-1	bal.	26	10	0
Alloy-2	bal.	26	10	0.6
Alloy-3	bal.	26	10	1.7

solution-treated at 1200 °C for 100 h, and air-cooled. All nominal compositions are listed in Table 1.

Prior to oxidation, the alloy surfaces were ground using 320, 600, and 1200 grit SiC paper to ensure a flat and uniform surface, and then polished using 6, 3, and 1  $\mu\text{m}$  diamond slurries. For the isothermal oxidation experiments, samples were placed in an alumina boat inside a quartz tube. Samples were first heated to 1000 °C in pure Ar gas. Once at temperature, O<sub>2</sub> gas was introduced and samples were oxidized in a 20% O<sub>2</sub>–Ar atmosphere for set times ranging from 5 min to 32 h.

Oxide scale surfaces and cross sections were characterized using a FEI Helios 650 NanoLab scanning electron microscope (SEM) and focused ion beam (FIB) and FEI Nova 200 NanoLab SEM/FIB. Wavelength-dispersive spectroscopy (WDS) was performed using a Cameca SX100 Electron Probe Microanalyzer using Cr, Al, Ti, and NiAl metal reference samples. Electron-transparent cross-section lamellae were prepared using a standard FIB lift-out and thinning technique. Electron microscopy imaging, electron diffraction, and energy-dispersive spectroscopy (EDS) was performed on a JEOL 2010F Analytical Electron Microscope with 200 kV accelerating voltage, equipped with an EDAX Sapphire Si-Li X-ray detector and EDAX Genesis software. Atom probe tomography (APT) needle-shaped specimens were prepared using standard FIB lift-out and milling procedures. APT analysis was carried out on a Cameca LEAP 4000X HR Atom Probe instrument operated in laser mode with a laser energy of 50 pJ, detection rate of 0.005 atoms/pulse, and a pulse rate of 200 kHz, with samples cooled to 50 K. APT data reconstruction and analysis were done with Cameca IVAS software version 3.6.12.

## Results

The as-received alloys were polycrystalline with grain sizes around 100–200  $\mu\text{m}$  for Alloys 1–3. In the Ti-containing alloys, a  $\gamma + \gamma'$  microstructure was observed, with an average  $\gamma'$  particle radius of 45.7 nm for the Alloy 2 and 65.2 nm for the Alloy 3 (Fig. 2a). Considering the size of the  $\gamma'$  particles, and the calculated  $\gamma'$  solvus temperature of 1012 °C and 1080 °C in the low-Ti and high-Ti alloy, respectively, it is likely that  $\gamma'$  formed upon cooling after the solution treatment at 1200 °C. These  $\gamma'$  precipitates were observed below a depletion zone under the oxide scale, and coarsened slowly as oxidation progressed, but are not thought to significantly affect oxidation behavior. Additionally, large, faceted TiN particles could be seen in both Ti-containing alloys prior to oxidation (Fig. 2b).

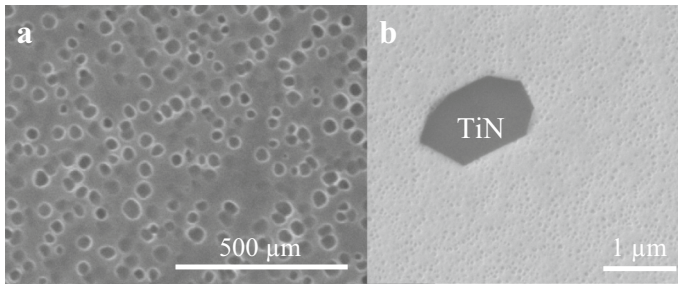


**Fig. 2** SEM images from the as-received Ni–26Cr–10Al–0.6Ti alloy: **a**  $\gamma + \gamma'$  and **b** TiN particle. Images were taken using a through lens detector (TLD) in secondary electron (SE) mode, with a 2 kV accelerating voltage

The oxidation of Alloy 1 (Ni–26Cr–10Al) revealed oxide thicknesses and morphologies varying significantly across the surface of the alloy, and correlating with an inhomogeneous Al distribution throughout the alloy, despite solution treatment. As illustrated in Fig. 3 in the low-Al regions, with Al concentrations as low as  $\sim 6.7$  at.% Al, long, discontinuous alumina fingers and an overall thicker oxide scale formed after oxidation for 32 h at 1000 °C. Alternatively, a compact, continuous alumina layer and overall thinner oxide scale formed in the high-Al regions, containing 9.5 at.% Al on average. Comparatively, no Al concentration inhomogeneity

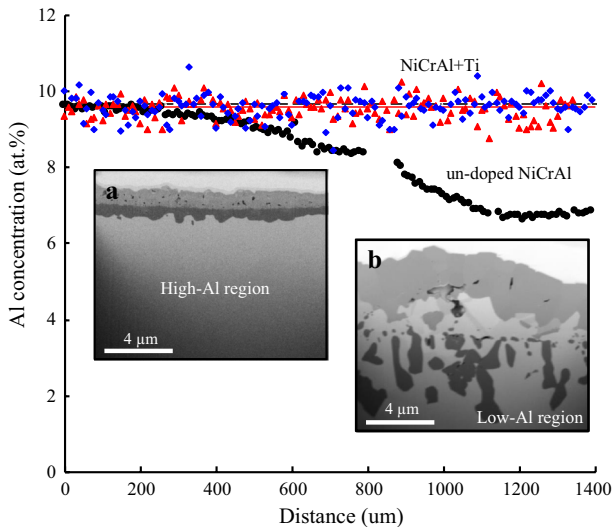


**Fig. 3** WDS composition profiles parallel to the alloy surface, measured approximately 400  $\mu\text{m}$  below the scale, showing the aluminum content across the matrix region in all 3 alloys, after oxidation at 1000 °C for 32 h. The right side of the line scan shows a region of low Al content typical in the as-received un-doped NiCrAl alloys, while no such regions were observed in the Ti-containing alloys. SEM images, taken using a TLD detector in backscatter electron mode with 2 kV accelerating voltage, of the oxide scale observed on the un-doped Ni–26Cr–10Al alloy in both the high (**a**) and low-Al (**b**) regions are presented for comparison

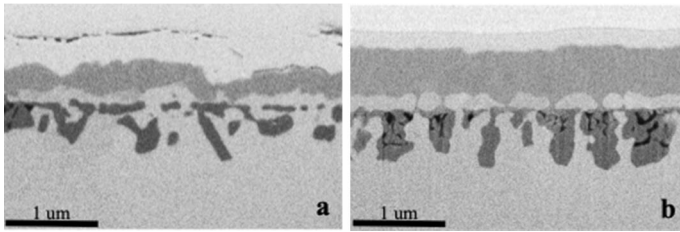


**Fig. 4** SEM image of FIB cross section of **a** Alloy 1 and **b** Alloy 3, oxidized at 1000 °C for 5 min. Images were taken using a TLD detector in BSE mode, with an accelerating voltage of 2 kV

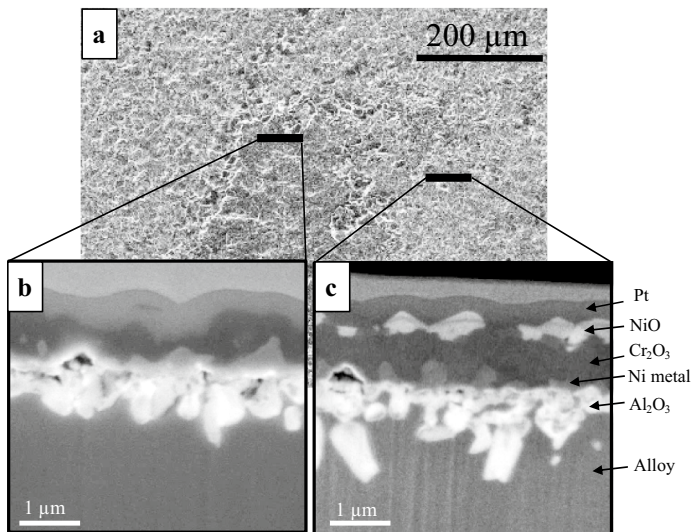


**Fig. 5** SEM images of Ni-26Cr-10Al alloy oxidized at 1000 °C for 30 min, showing cross sections from two different surface contrast regions. Cross-sectional images are taken from **b** the “dark” region seen on the surface and **c** the “bright” region. Images were taken using a TLD detector in SE mode, with an accelerating voltage of 5 kV

was observed in the Ti-containing alloys that exhibited uniform Al distribution with concentrations comparable to those in the high-Al regions of the un-doped alloy. According to early work on the oxidation of the Ni–Cr–Al system [1, 17], the critical Al content at which the oxide scale transitions from discontinuous internal alumina precipitates to a continuous  $\text{Al}_2\text{O}_3$  scale occurs around 10 at.% Al for alloys containing 26 at.% Cr, and small changes in Al concentration near this critical value may have a significant effect on oxidation behavior. For the remainder of this study, we focus exclusively on regions of high Al content in Alloy 1 when comparing to the Ti-containing Alloys 2 and 3, to distinguish the effect of Ti doping from effects of Al concentration.

Starting with Alloy 1 after 5 min of oxidation at 1000 °C, a continuous  $\text{Cr}_2\text{O}_3$  layer was observed in cross section (Fig. 4a), below which discontinuous  $\text{Al}_2\text{O}_3$



“fingers” formed deeper into the alloy. After 30 min of oxidation, the oxide scale revealed two different regions distinguished by their surface imaging contrast (bright and dark in Fig. 5a). These regions did not correlate with the Al compositional fluctuations and were present in both the low and high Al portions of the alloy. In the “bright” scale regions, a multilayered scale formed, consisting of (from top to bottom) discontinuous islands of NiO on the surface, a continuous layer of  $\text{Cr}_2\text{O}_3$ , Ni-rich metal grains, and an  $\text{Al}_2\text{O}_3$  layer with fingers extending into the alloy (Fig. 5c). In the “dark” scale regions (Fig. 5b), the same phases and morphology were present with the exception of the NiO islands. Oxide phases were identified by EDS analyses and in the case of the  $\text{Cr}_2\text{O}_3$  and  $\text{Al}_2\text{O}_3$  phases, by additional selected area electron diffraction. Large pores were also visible between the  $\text{Cr}_2\text{O}_3$  and  $\text{Al}_2\text{O}_3$  layers among the Ni metal grains that contained  $\sim 5$  at% Cr and  $< 1$  at.% Al, as estimated by EDS. After 2 h of oxidation, two regions were still visible on the surface, with the “dark” regions still lacking NiO on the surface. The  $\text{Al}_2\text{O}_3$  transitioned to a more continuous layer. Discontinuous  $\text{Cr}_2\text{O}_3$  grains, rather than a continuous  $\text{Cr}_2\text{O}_3$  layer, were observed within a Ni- and Cr-rich oxide layer (Fig. 6b) that had a composition consistent with that of the  $\text{NiCr}_2\text{O}_4$  phase. A representative EDS mapping analysis used to distinguish the oxide phases within the scale is shown in Fig. 7, along with a concentration profile across the scale. Finally, we also note that the Ni-rich metal grains observed after 30 min were replaced by large voids and grains of  $\text{NiCr}_2\text{O}_4$ . After 8 h of oxidation, the same phases (NiO,  $\text{NiCr}_2\text{O}_4$ ,  $\text{Cr}_2\text{O}_3$ , and  $\text{Al}_2\text{O}_3$ ) were present, with few isolated grains of NiO on the surface. The distinct contrast regions were no longer observed. The alumina layer thickened slightly to become more uniform. A continuous  $\text{Cr}_2\text{O}_3$  layer was identified directly above the  $\text{Al}_2\text{O}_3$

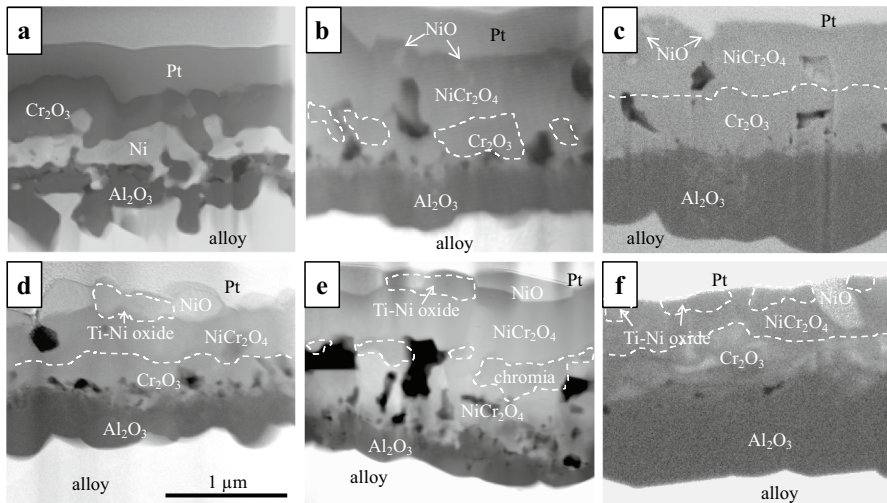


**Fig. 6** Cross-sectional SEM images, taken using ETD detector in SE mode with 2 kV accelerating voltage, of Ni-26Cr-10Al alloy (a–c) and Ni-26Cr-10Al-1.7Ti alloy (d–f) oxidized at 1000 °C for 30 min, 2 h, and 32 h at the same magnification. Oxide phases are labeled, and in some cases outlined, for increased clarity

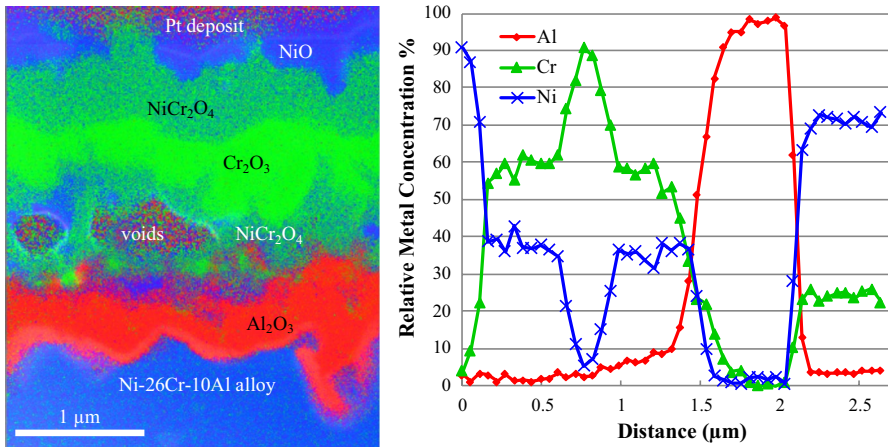


**Fig. 7** Combined EDS map (left) of scale cross section from Ni–26Cr–10Al oxidized for 2 h at 1000 °C, with Al shown in red, Cr shown in green, and Ni shown in blue (oxygen content is not shown). A qualitative EDS profile of the relative metal composition of Ni, Cr, and Al perpendicular to the alloy surface from the top surface of the scale into the alloy is shown to the right

layer. A NiCr<sub>2</sub>O<sub>4</sub> layer was still present above the Cr<sub>2</sub>O<sub>3</sub> layer. After 32 h of oxidation (Fig. 6c), the Al<sub>2</sub>O<sub>3</sub> layer had thickened, while the combined thickness of the NiCr<sub>2</sub>O<sub>4</sub> and Cr<sub>2</sub>O<sub>3</sub> layers did not appear to grow, and only occasional NiO grains on the top surface of the scale remained.

Upon oxidation of the Ti-doped Ni–26Cr–10Al alloys (Alloys 2 and 3), the same major oxide phases and relative oxide layer thicknesses as those present on the un-doped NiCrAl alloy (Alloy 1) were observed. Al<sub>2</sub>O<sub>3</sub> layer thickness at various oxidation times was similar for Alloys 1–3 (Fig. 8). However, the formation of Ti-rich phases at the surface of the scales grown on Alloys 2 and 3 at longer oxidation

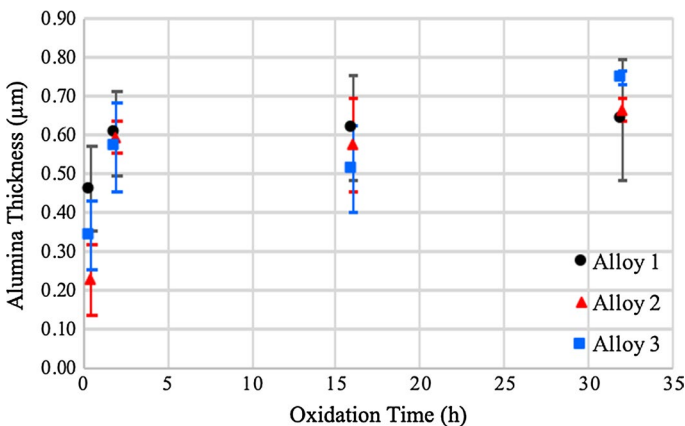


**Fig. 8** Average alumina layer thickness versus oxidation time at 1000 °C. Measurements were taken at several locations on each sample using FIB cross sections



times was noted. After 5 min at 1000 °C, a continuous  $\text{Cr}_2\text{O}_3$  layer formed on the surface, with discontinuous  $\text{Al}_2\text{O}_3$  fingers deeper underneath in the alloy (Fig. 4b). Compared to the Ti-free Alloy 1, the  $\text{Cr}_2\text{O}_3$  layers on Alloys 2 and 3 were slightly thicker ( $\sim 0.40\ \mu\text{m}$  vs  $0.25\ \mu\text{m}$ ), while the depth of the  $\text{Al}_2\text{O}_3$  fingers and the distance they had precipitated beneath the  $\text{Cr}_2\text{O}_3$  were nearly identical on Alloys 1–3. After 30 min at 1000 °C, two regions were observed. Similar to the scales on the un-doped alloys, the presence or absence of NiO grains on the surface of the oxide scale distinguished the two regions. The “bright region” consisted of NiO grains on the surface, a layer of  $\text{NiCr}_2\text{O}_4$ , and then a layer of  $\text{Cr}_2\text{O}_3$  above a thin, continuous  $\text{Al}_2\text{O}_3$  layer (Fig. 6d). The “dark region” consisted of the same phases but without NiO grains on the surface. On Alloy 2, a thin region of Ti enrichment on the scale surface was detected, and on Alloy 3, larger grains of a Ti–Ni-rich oxide were identified at the surface between the NiO grains where present. Large pores could also be seen in the  $\text{NiCr}_2\text{O}_4$  and  $\text{Cr}_2\text{O}_3$  layers, and smaller pores were visible near the top of the  $\text{Al}_2\text{O}_3$ .

Dispersed “nodules” were observed (Fig. 9a) on the surfaces of the Ti-containing Alloys 2 and 3 after 30 min of oxidation and grew in size as the oxidation time increased. The nodules consisted of a thick Ti–Ni-rich oxide protruding outward and inward above continuous  $\text{NiCr}_2\text{O}_4$ , chromia, and alumina layers (Fig. 9b). Small dark particles were observed locally under the nodules and were found, using APT, to be rich in Ti, N, and C. After 2 h of oxidation, away from the large nodules, NiO islands were still present on the surface, embedded in a layer of  $\text{NiCr}_2\text{O}_4$ . Again, a thin Ti-rich layer was detected at the surface of the scale of Alloy 2, and the Alloy 3 surface exhibited larger Ti–Ni-rich oxides (Fig. 6e). Discontinuous  $\text{Cr}_2\text{O}_3$  grains could be seen in the middle of the  $\text{NiCr}_2\text{O}_4$  on both alloys. APT analyses revealed that Ti segregated to grain and interphase boundaries within the chromia and  $\text{NiCr}_2\text{O}_4$  layers (Fig. 10). Below the  $\text{NiCr}_2\text{O}_4$  layer, a continuous  $\text{Al}_2\text{O}_3$  layer was slightly thicker and more continuous than that observed after 30 min of oxidation. Porosity was present in the lower part of the  $\text{NiCr}_2\text{O}_4$  layer and around the  $\text{Cr}_2\text{O}_3$  grains, and some smaller pores could still be seen near the top of the alumina. After 8 h of oxidation, the majority of the surface on both Ti-doped alloys was covered

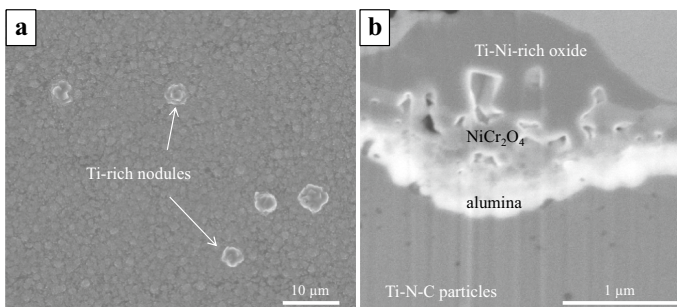
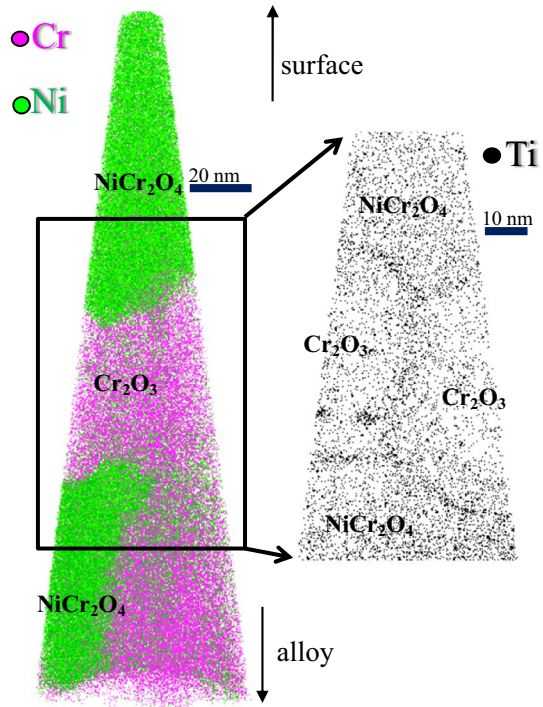


**Fig. 9** **a** SEM image of the surface of Alloy 3 oxidized for 2 h at 1000 °C. The Ti nodules could be seen on both of the Ti-containing alloys after 30 min of oxidation and grew with increasing oxidation time. **b** SEM cross-sectional image of a nodule, using a TLD detector in SE mode with 5 kV accelerating voltage

**Fig. 10** APT reconstruction of a volume prepared within the  $\text{Cr}_2\text{O}_3$  and  $\text{NiCr}_2\text{O}_4$  layers of a scale grown on the Ni–26Cr–10Al–0.6Ti alloy after 2 h of oxidation. In the reconstruction on the left, chromium ions are shown in pink and Ni ions are shown in green. In the 5-nm-thick slice on the right, Ti ions are shown in black



in the  $\text{NiCr}_2\text{O}_4$  layer, with interspersed embedded NiO grains. Below the  $\text{NiCr}_2\text{O}_4$  layer, a continuous layer of  $\text{Cr}_2\text{O}_3$  was present, and the continuous alumina layer had grown thicker. Porosity was observed in the  $\text{NiCr}_2\text{O}_4$  layer near the  $\text{NiCr}_2\text{O}_4$ –chromia interface. After 32 h, extensive spalling was visible on the alloy surfaces. On the remaining oxide, the  $\text{NiCr}_2\text{O}_4$  and  $\text{Cr}_2\text{O}_3$  layers were still present, and the  $\text{Al}_2\text{O}_3$  layer had grown noticeably thicker (Fig. 6f). Scarce NiO particles remained on each surface, while the Ti–Ni-rich oxide grains grew on the scale surfaces of the high-Ti alloy.

## Discussion

The overall behavior and scale evolution described here, i.e., the development of a continuous  $\text{Al}_2\text{O}_3$  layer below a  $\text{Cr}_2\text{O}_3$  layer observed for Alloys 1–3, is consistent with previous work by Giggins and Pettit [1], Nijdam et al. [18, 19] and Hu et al. [20] on transient oxidation of alloys with similar composition (Ni-(26–30) % Cr-(8–11)%Al). However, the observations and interpretations of the very initial development of the oxide scale differ. In the current study, observations of the oxide scale after 5 min at 1000 °C (Fig. 4) revealed that initially an outer layer of  $\text{Cr}_2\text{O}_3$  formed, with discontinuous  $\text{Al}_2\text{O}_3$  particles below, in agreement with Hu et al. [20]. The initial formation of  $\text{Cr}_2\text{O}_3$  depleted the alloy of Cr. The continuous  $\text{Cr}_2\text{O}_3$  layer also contained a non-negligible amount of Al (~7 at.% Al measured by APT), resulting

in the depletion of aluminum in the alloy directly below the  $\text{Cr}_2\text{O}_3$  layer. Consequently, internal  $\text{Al}_2\text{O}_3$  grains precipitated at a fixed distance beneath this depletion layer as oxygen diffused into the alloy [21]. The  $\text{Al}_2\text{O}_3$  grains continued to grow into the alloy to form elongated “fingers” (Figs. 3b, 4, 5). Elongated  $\text{Al}_2\text{O}_3$  precipitates are well documented in the literature, and their evolution depends on the relative fluxes of aluminum and oxygen at the inner  $\text{Al}_2\text{O}_3$ /metal interface [22]. The thickening  $\text{Cr}_2\text{O}_3$  layer reduced the oxygen flux through the scale and into the alloy with time, allowing Al to diffuse to the scale–alloy interface and form additional  $\text{Al}_2\text{O}_3$  grains rather than grow the  $\text{Al}_2\text{O}_3$  fingers. Eventually, a continuous layer formed, as also reported in [2, 22]. The coalescence into a dense, continuous layer trapped the depleted Ni metal above, which is consistent with prior observations [18, 20]. An alternate explanation for the trapped Ni metal comes from extrusion of soft, depleted nickel upon the volume increase associated with  $\text{Al}_2\text{O}_3$  formation [23, 24]. This creep mechanism might drive the transport of metal to the scale surface for dilute binary alloys that form single-phase scales, but in the case of ternary alloys that form multiple oxide layers, it seems unlikely extrusion would occur. Additionally, the thicknesses of trapped Ni were similar for the Ni–26Cr–10Al alloy oxidized for 10 min and for 30 min (Fig. 11), despite significant differences in  $\text{Al}_2\text{O}_3$  morphology.

After some time, NiO particles formed on regions of the scale surface above the  $\text{Cr}_2\text{O}_3$ , as previously reported [20]. As oxidation progressed, a layer of  $\text{NiCr}_2\text{O}_4$  formed between the NiO and  $\text{Cr}_2\text{O}_3$ . This layer is inferred to occur by solid-state reaction between diffusing Ni from the Ni pockets trapped between the  $\text{Cr}_2\text{O}_3$  and  $\text{Al}_2\text{O}_3$  and the  $\text{Cr}_2\text{O}_3$  layer. We hypothesize that the depleted Ni grains evolved by two mechanisms. Ni diffused to the surface, feeding the outer NiO and  $\text{NiCr}_2\text{O}_4$  layers, in agreement with [18, 20]. This upward diffusion is consistent with the formation of large voids between the  $\text{Cr}_2\text{O}_3$  and  $\text{Al}_2\text{O}_3$  observed at intermediate oxidation times (2 and 8 h) and the growth of the  $\text{NiCr}_2\text{O}_4$  layer above the  $\text{Cr}_2\text{O}_3$  layer. The trapped Ni metal also oxidized and further transformed by solid-state reaction with the nearby  $\text{Cr}_2\text{O}_3$  phase to form  $\text{NiCr}_2\text{O}_4$  below the  $\text{Cr}_2\text{O}_3$ , as previously reported [20]. This is possibly enabled by concurrent upward Cr diffusion and downward

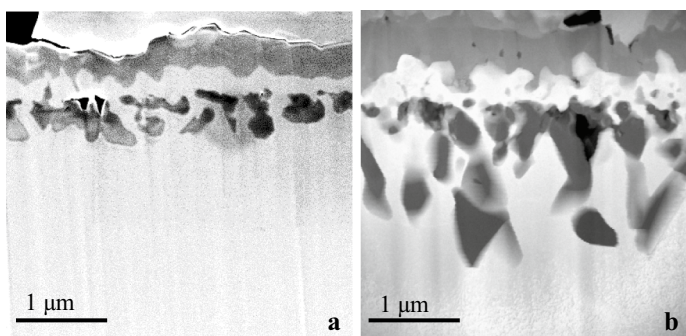


**Fig. 11** STEM dark-field images of FIB cross sections of the Alloy 1 oxidized for **a** 10 min and **b** 30 min at 1000 °C. The ratio of area of alumina to area of trapped Ni in each image is 1.6 for (a) and 2.5 for (b)

oxygen diffusion. Thermodynamically,  $\text{NiCr}_2\text{O}_4$  was not expected to form below  $\text{Cr}_2\text{O}_3$  since it is relatively less stable [25].  $\text{NiCr}_2\text{O}_4$  likely formed in this region at short oxidation times for kinetic reasons or due to a shallow gradient of oxygen activity maintained through a region with large pores. We note that in addition to the spatial re-arrangements of the oxide phases following the establishment of  $P_{\text{O}_2}$  gradient, the thickening of the  $\text{NiCr}_2\text{O}_4$  and  $\text{Cr}_2\text{O}_3$  layers also required upward Ni and Cr fluxes from the alloy through the continuous  $\text{Al}_2\text{O}_3$ ,  $\text{Cr}_2\text{O}_3$ , and  $\text{NiCr}_2\text{O}_4$  layers.

The present results suggest that Ti additions do not have a significant effect on the overall scale thickness or the major oxide phases formed and their morphologies up to 32 h of oxidation. At the shortest oxidation times, before a continuous  $\text{Al}_2\text{O}_3$  layer was formed, the Ti-doped alloys exhibited thicker layers of  $\text{Cr}_2\text{O}_3$ , consistent with prior claims that Ti accelerates the kinetics of  $\text{Cr}_2\text{O}_3$  layer growth [8–10]. However, the  $\text{Al}_2\text{O}_3$  growth kinetics upon formation of a continuous layer were not significantly changed by Ti (Fig. 8). The Ti-enriched surface and Ti-rich oxides observed on the surfaces of the scales grown on the Ti-containing alloys indicated that Ti actively diffused toward the scale surface along grain boundaries and interfaces. This is consistent with a “reactive element”-type effect [26]; however,  $\text{NiCr}_2\text{O}_4$ ,  $\text{Cr}_2\text{O}_3$ , or  $\text{Al}_2\text{O}_3$  growth kinetics did not seem to be affected when comparing the scales on the Ti-free and Ti-containing alloys. Prior work on Fe–20Cr–10Al (at.%) alloys also concluded that titanium does not have a significant effect on alumina growth kinetics [11]. On the other hand, the discrepancy with Santoro *et al.*'s conclusions [23] that Ti changes the oxidation kinetics of  $\gamma$ -Ni–10Al alloys may be explained by differences in alloy composition; without Cr, the level of aluminum required to transition to a continuous scale rather than internal precipitates is much higher, so the phases and morphology of the oxide scale formed were significantly different than those seen in the current study. When comparing alloys close to the transition for continuous  $\text{Al}_2\text{O}_3$  growth, the oxidation behavior is much more sensitive to the aluminum concentration and any fluctuation in Al concentration than the small additions of Ti. Finally, it is worth noting that for the alloys studied here, weight gain measurements alone would have led to inaccurate conclusions. The behavior of the un-doped alloy would have been dominated by the low-Al regions which do not form a continuous alumina layer, giving the appearance of a strong, beneficial Ti effect on oxidation behavior.

One significant difference in oxidation behavior of the Ti-containing alloys was the formation of Ti-rich oxides at the scale/gas interface, and localized Ti-rich oxide nodules. The dispersed TiN particles observed on the un-oxidized alloys were of similar number density and size as the nodules observed on the surface of the oxidized samples (Fig. 9a). As these particles oxidized, it is likely that increased local oxidation occurred due to cracking caused by the large volume change as TiN transformed to  $\text{TiO}_2$  [27–29]. During oxidation of the TiN particles, some nitrogen was rejected into the matrix. Small Ti–N–C particles then precipitated in the matrix under the scale in the areas of nitrogen enrichment. These particles below the scale became enveloped by the inward growing  $\text{Al}_2\text{O}_3$  layer over time. The local variations in scale thickness around the Ti-rich nodules could result in stresses in the scale and likely contributed to the accelerated spallation behavior of the titanium-doped alloys. Several superalloy and coating studies [8, 30–32] previously observed

growth of titanium oxides on the surface of the scales and increased spalling behavior with higher Ti content. This is consistent with the design trend of reducing the titanium content to improve oxidation behavior of modern superalloys. The qualitatively inferior spalling behavior observed on the Ti alloys at longer oxidation times in the current study seems to justify this trend.

## Conclusions

The scales developing on four model alloys, Ni–26Cr–10Al–(0,0.6,1.7)Ti (at%) and Ni–26Cr–12Al, during oxidation at 1000 °C in a 20% O<sub>2</sub>–Ar atmosphere were characterized using scanning electron microscopy, transmission electron microscopy, and atom probe tomography. The following conclusions were reached:

- On the un-doped NiCrAl alloys, NiO, NiCr<sub>2</sub>O<sub>4</sub>, Cr<sub>2</sub>O<sub>3</sub>, and Al<sub>2</sub>O<sub>3</sub> layers formed and developed over time, consistent with previous studies on the transient oxidation of alloys of similar composition. In regions of the alloy with low Al composition, internal alumina fingers formed which extended into the alloy, while in regions with high Al composition, the alumina transitioned into a continuous layer which grew with increasing oxidation time.
- For similar Al and Cr composition in the base alloy, Ti addition did not affect the kinetics and morphology of the protective oxide phases (Al<sub>2</sub>O<sub>3</sub> and Cr<sub>2</sub>O<sub>3</sub>) in the early stages of oxidation, up to 32 h at 1000 °C.
- Ti diffused upward toward the scale/gas interface along interfaces and grain boundaries within the oxide scale, becoming enriched at the scale surface and forming Ti-rich oxides with sufficient Ti level in the alloy.
- TiN particles present in the Ti-doped alloys oxidized and experienced large increases in volume, leading to thick local oxide “nodules” which are potentially starting sites for scale spallation.

**Acknowledgements** The authors also acknowledge funding from the National Science Foundation under Grant DMR-1352157, and instrument access and technique support from the Michigan Center for Materials Characterization and the Robert B. Mitchell Electron Microbeam Analysis Laboratory at the University of Michigan. The authors would like to thank Prof. Roger Reed and Dr. Yilun Gong at the University of Oxford for initial discussions and for providing Alloys 1, 2, and 3.

## References

1. F. S. Pettit and C. S. Giggins, *Journal of the Electrochemical Society: Solid State Science*. **118**, 1782 (1971).
2. D. J. Young, *High Temperature Oxidation and Corrosion of Metals*, (Elsevier, Amsterdam, 2016).
3. D. Naumenko, B. A. Pint and W. J. Quadackers, *Oxidation of Metals* **86**, 1 (2016).
4. P. Y. Hou, *Journal of the American Ceramic Society*. **86**, 660 (2003).
5. H. Liu, M. M. Stack and S. B. Lyon, *Solid State Ionics* **109**, 247 (1998).
6. F. H. Stott, G. B. Wood and J. Stringer, *Oxidation of Metals* **44**, 113 (1995).

7. R. C. Reed, *The Superalloys: Fundamentals and Applications*, (Cambridge University Press, Cambridge, 2006).
8. S. Cruchley, H. E. Evans, M. P. Taylor, M. C. Hardy and S. Stekovic, *Corrosion Science* **75**, 58 (2015).
9. P. K. Arve Holt, *Solid State Ionics* **117**, 21 (1999).
10. N. Aran, A. A. Blacklocks, R. J. Packer, S. L. P. Savin and A. V. Chadwich, *Solid State Ionics*. **177**, 2939 (2006).
11. B. A. Pint and K. B. Alexander, *Journal of the Electrochemical Society* **145**, 1819 (1998).
12. B. A. Pint, M. Treska and L. W. Hobbs, *Oxidation of Metals*. **47**, 1 (1997).
13. G. J. Santoro, D. L. Deadmore, C. E. Lowell, Oxidation of Alloys in Nickel-Aluminum System with Third-Element Additions of Chromium, Silicon, and Titanium at 1100 C. *NASA Technical Note* (1971).
14. D. Clemens, W. J. Quadakkers and L. Singheiser, *Electrochemical Society Proceedings* **98-9**, 134 (1998).
15. D. Naumenko, V. Kochubey, L. Niewolak, A. Dymiati, J. Mayer, L. Singheiser and W. J. Quadakkers, *Journal of Materials Science*. **43**, 4550 (2008).
16. B. A. Pint and K. A. Unocic, *Materials at High Temperatures*. **29**, 257 (2012).
17. G. R. Wallwork and A. Z. Hed, *Oxidation of Metals*. **3**, 171 (1971).
18. T. J. Nijdam, N. M. van der Pers and W. G. Sloof, *Materials and Corrosion*. **57**, 269 (2006).
19. T. J. Nijdam, L. P. H. Jeurgens and W. G. Sloof, *Materials at High Temperatures*. **20**, 311 (2003).
20. L. Hu, D. B. Hovis and A. H. Heuer, *Oxidation of Metals*. **73**, 275 (2010).
21. T. J. Nijdam, L. P. H. Jeurgens and W. G. Sloof, *Acta Materialia*. **53**, 1643 (2005).
22. R. A. Rapp, Kinetics, Microstructures and Mechanism of Internal Oxidation- Its Effect and Prevention in High Temperature Alloy Oxidation. *21st Conference, National Association of Corrosion Engineers*, St. Louis, MO, (1965).
23. H. C. Yi, S. W. Guan, W. W. Smeltzer and A. Petric, *Acta Metallurgica et Materialia* **42**, 981 (1994).
24. F. H. Stott and G. C. Wood, *Materials Science and Technology*. **4**, 1072 (1988).
25. G. M. Kale and D. J. Fray, *Metallurgical and Materials Transactions B*. **25B**, 373 (1994).
26. B. A. Pint, *Oxidation of Metals*. **45**, 1 (1996).
27. W. J. Quadakkers, D. Naumenko, L. Singheiser, H. J. Penkalla, A. K. Tyagi and A. Czyska-Filemonowicz, *Materials and Corrosion*. **51**, 350 (2000).
28. L. Huang, X. F. Sun, H. R. Guan and Z. Q. Hu, *Tribology Letters*. **23**, 15 (2006).
29. J. Litz, A. Rahmel and M. Schorr, *Oxidation of Metals*. **30**, 95 (1988).
30. J. H. Chen, P. M. Rogers and J. A. Little, *Oxidation of Metals*. **47**, 381 (1997).
31. R. J. Bennett, R. Krakow, A. S. Eggeman, C. N. Jones, H. Murakami and C. M. F. Rae, *Acta Materialia*. **92**, 278 (2015).
32. J. A. Haynes, K. A. Unocic, M. J. Lance and B. A. Pint, *Oxidation of Metals*. **86**, 453 (2016).

**Publisher's Note** Springer Nature remains neutral with regard to jurisdictional claims in published maps and institutional affiliations.

## Affiliations

Talia L. Barth<sup>1</sup> · Emmanuelle A. Marquis<sup>1</sup> 

✉ Emmanuelle A. Marquis  
emarq@umich.edu

<sup>1</sup> Department of Materials Science and Engineering, University of Michigan, Ann Arbor, MI, USA